

Banner appropriate to article type will appear here in typeset article

Fast droplet impact onto slowly moving deep pools

Thomas C. Sykes^{1,2}, Luke F.L. Alventosa³, J. Rafael Castrejón-Pita⁴,
Radu Cimpeanu⁵, Daniel M. Harris³, and Alfonso A. Castrejón-Pita²

¹School of Engineering, University of Warwick, Coventry CV4 7AL, UK

²Department of Engineering Science, University of Oxford, Oxford OX1 3PJ, UK

³School of Engineering, Brown University, Providence, RI 02912, USA

⁴Department of Mechanical Engineering, University College London, London WC1E 7JE, UK

⁵Mathematics Institute, University of Warwick, Coventry CV4 7AL, UK

Corresponding author: Thomas C. Sykes, thomas.sykes@warwick.ac.uk and t.c.sykes@outlook.com

(Received xx; revised xx; accepted xx)

When a fast droplet impacts a pool, the resulting ejecta sheet dynamics determine the final impact outcome. At low Capillary numbers, the ejecta sheet remains separate from a deep static pool, whilst at higher viscosities it develops into a lamella. Here, we show that the common natural scenario of a slowly moving deep pool can change the upstream impact outcome, creating highly three-dimensional dynamics no longer characterised by a single descriptor. By considering how pool movement constrains the evolution of the ejecta sheet angle, we reach a length-scale invariant parameterisation for the upstream transition that holds for a wide range of fluids and impact conditions. Direct numerical simulations show similar dynamics for an equivalent oblique impact, indicating that the pool boundary layer does not play a decisive role for low pool-droplet speed ratios. Our results also provide insight into the physical mechanism that underpins pool impact outcomes more generally.

1. Introduction

Most droplet impact research concerns normal collisions with a static substrate. However, in many natural and industrial processes, droplets impact obliquely or onto a moving substrate. This seemingly subtle distinction transforms droplet impact from the typical axisymmetric configuration to be inherently three-dimensional (3D). Example processes include raindrop splashing on the moving ocean that contributes to air–sea exchange ([Anguelova 2021](#)), inkjet printing onto moving paper ([Lohse 2022](#)), and crop spraying with numerous droplet impacts at arbitrary angles ([Gielen *et al.* 2017](#)).

Most of the existing literature on moving substrates has considered dry surfaces, where horizontal surface motion can modify splashing thresholds ([Bird *et al.* 2009](#); [Hao & Green 2017](#)), alter spreading factors ([Li *et al.* 2024](#)), and even generate new impact outcomes like boundary layer-driven “aerodynamic rebound” ([Stumpf *et al.* 2025](#)). Likewise, inclined static surfaces yield asymmetric crowns and reduce splashing propensity ([Hao *et al.* 2019](#)).

Fluid (short name)	Density, ρ (kg m ⁻³)	Dyn. viscosity, μ (mPa s)	Surface tension, σ (mN m ⁻¹)
Distilled water	997 ± 1	0.93 ± 0.01	72.4 ± 0.2
21 vol% glycerol-water	1058 ± 1	1.9 ± 0.0	71.0 ± 0.3
32 vol% glycerol-water	1089 ± 1	3.0 ± 0.1	70.3 ± 0.2
43 vol% glycerol-water	1122 ± 1	5.4 ± 0.2	69.0 ± 0.4
47 vol% glycerol-water	1134 ± 2	6.5 ± 0.3	68.4 ± 0.5
51 vol% glycerol-water	1145 ± 2	8.0 ± 0.3	67.8 ± 0.4
1 cSt silicone oil	816	0.8	17.4
2 cSt silicone oil	870	1.7	18.7

Table 1. Fluid properties of the droplet and pool (same fluid). The density of each glycerol-water mixture (glycerol, Acros Organics 99% pure) was measured using a 25 mL density bottle and 1 mg precision analytical balance, dynamic viscosity with a vibrational viscometer (Hydramotion Viscolite 700, 0.1 mPa s precision), and surface tension with a Sinterface BPA-2S tensiometer. Measured viscosities were confirmed to be consistent with known empirical correlations (Cheng 2008). Silicone oils (Clearco Products) were used as received; the fluid properties reported are those from the product data sheet. All values are reported for 23 ± 1 °C.

When the substrate is a pool, either moving or with a droplet impacting obliquely, the literature is more limited and exploratory. Castrejón-Pita *et al.* (2016) identified distinct regimes (including a new ‘surfing’ outcome) that depend on the droplet-pool speed ratio, but could not explore low pool speeds. Several studies have considered thin films that are either flowing (Guo *et al.* 2025) or obliquely impacted (Bao *et al.* 2025). A few authors have considered oblique impact (Gielen *et al.* 2017; Reijers *et al.* 2019), and moving (Gupta & Kumar 2020), deep pools. However, all of these works focused on long time-scale dynamics such as crater evolution, crown structure, and the Worthington jet.

For static pools, following the observation that high-speed droplet impact leads to the formation of an ejecta sheet (Weiss & Yarin 1999; Thoroddsen 2002), it is now well understood that the ejecta sheet dynamics on very short time scales determine impact outcomes (Wang *et al.* 2023). On a deep pool, the ejecta sheet may collect fluid from the pool and form a lamella, or remain separate (separate ejecta sheet, SES); the transition between these regimes is associated with a fixed Capillary number, $Ca = 0.2$ (Agbaglah *et al.* 2015). Herein, we extend this knowledge to include pool movement and show that impact outcomes can differ upstream and downstream only when $Ca < 0.2$. The transition can be explained by considering the evolution of the ejecta sheet angle, giving a length-scale invariant parametrisation of Ca and the square root of the pool-droplet velocity ratio.

2. Methods

2.1. Experiments

Millimetric droplets were dripped from a blunt end dispensing tip and impacted normally onto a deep pool, both consisting of the same fluid: distilled water, five glycerol-water mixtures, and two silicone oils – see table 1. Six dispensing tips (15–30 gauge, outer diameters 0.31–1.83 mm) were used to modify the droplet diameter $D \in [2.20, 3.75]$ mm, which is our characteristic length scale measured by the circle-fitted nominal radius, r_n (see the supplementary material). The dispensing tip height relative to the pool free surface was varied (205–575 mm) to adjust the normal impact velocity, $u_n \in [1.6, 3.2]$ m s⁻¹. The variation in u_n was primarily responsible for the range of $We = \rho u_n^2 D / \sigma \in [134, 450]$, while the different fluids enabled considerable variation in $Re = \rho u_n D / \mu \in [940, 7930]$ (figure 1a). As the Capillary number $Ca = We / Re = \mu u_n / \sigma$ proves influential, we non-dimensionalise times with the visco-capillary time scale, $\mu D / \sigma$ (denoted t_μ^*).

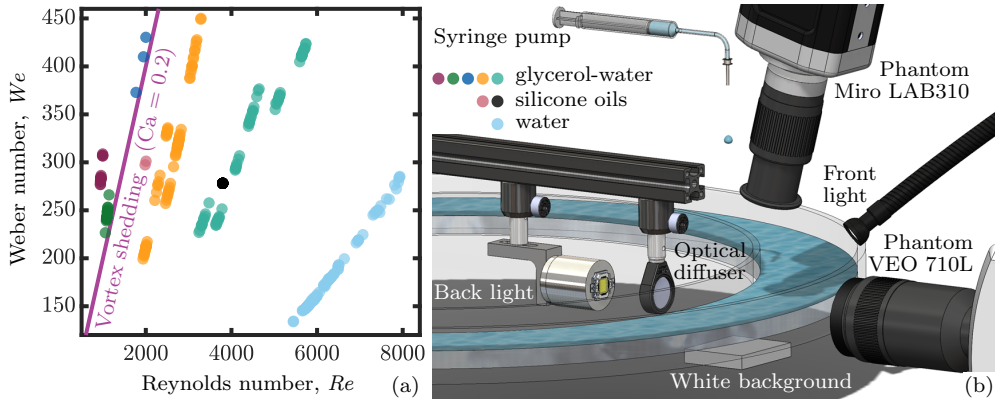


Figure 1. (a) We versus Re for all experiments reported. The purple line delineates the known vortex shedding boundary ($Re = 5We$, i.e. $Ca = 0.2$, [Agbaglah et al. 2015](#)). (b) A rendering of the experimental setup.

For all experiments, the pool depth h was maintained such that $h/D > 3$ (typically with $h \in [12, 14]$ mm), which is sufficient that the pool can be considered deep for the early-time dynamics of interest here ([Thoroddsen et al. 2011](#); [Sykes et al. 2023](#)). Pool movement was achieved using a belt-driven rotating table fitted with an optically clear annular tank (figure 1b), whose dimensions are specified in the supplementary material. The inner walls were treated with a commercial hydrophobic coating (Rain-X Plastic Water Repellent) to curtail the formation of a meniscus that would interfere with side-view imaging. The experiments involving silicone oils used a similar setup described in [Harris et al. \(2025\)](#).

Practical limitations restricted the maximum rotational frequency to around 0.5 Hz, with linear pool speeds at the impact point of $u_t \in [0, 0.6]$ m s⁻¹ reported here. u_t was calculated from the rotation rate of the table, which was determined by monitoring the time for each quarter rotation using an optical switch (Optek OPB900W55Z) connected to a data logger (Moku:Go). The implied u_t therefore assumes that the fluid is in solid body rotation with the tank and that the effect of air drag on the free surface is negligible. Consequently, a spin-up time of approximately 5 min was applied prior to all experiments, which is sufficient according to analysis of the typical timescales associated with the bottom-wall Ekman layer that is responsible for spin-up here ([Greenspan & Howard 1963](#); [Homicz & Gerber 1987](#)). Particle tracking velocimetry experiments were also used to verify the actual free surface velocities – see the supplementary material for both ([Crocker & Grier 1996](#)).

Impacts were imaged from the side (through the tank side wall, figure 1b) with a Phantom VEO 710L high-speed camera (7500–14,000 fps; 3–12 μ s exposure) in a shadowgraphy configuration, using a Laowa 100 mm lens (64–89 pixels mm⁻¹). A second front-lit high-speed camera (Phantom Miro LAB310; 4800–6300 fps; 40–70 μ s exposure), mounted 15° from vertical to keep the path of the falling droplet free, simultaneously imaged from an oblique viewpoint using a Tamron SP AF 90 mm lens (30–40 pixels mm⁻¹).

2.2. Direct numerical simulation

We constructed a high-fidelity computational counterpart of our system using the Basilisk open-source environment ([Popinet 2009, 2015](#)), which has been successfully used in recent years for supporting both experimental and theoretical high-speed droplet impact research to gain additional physical insight into rapidly evolving ejecta sheet dynamics ([Fudge et al. 2023](#); [Sykes et al. 2023](#)). The computational box is three-dimensional, with a symmetry boundary condition used on the plane spanned by the pool and droplet velocity vectors (figure 2(a)). The non-symmetry boundaries are $5r_n$ from the impact point, with either

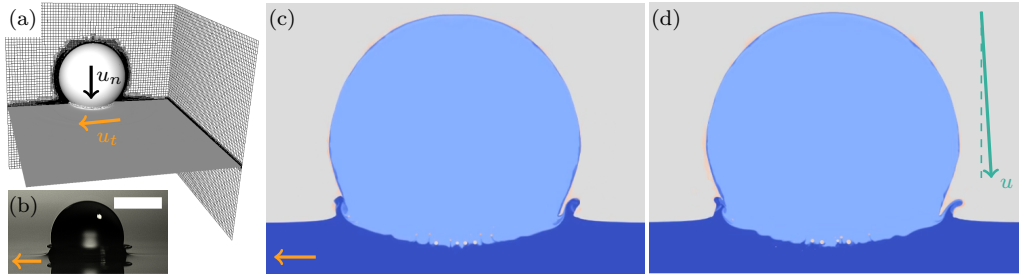


Figure 2. (a) Computational box highlighting adaptive grid refinement. (b) Experimental view of the case described by $Ca = 0.105$ (32 vol% fluid) and $u_t = 0.15 \text{ m s}^{-1}$ ($u_n = 2.45 \text{ m s}^{-1}$, $\sqrt{u_t/u_n} = 0.25$), at $t_\mu^* = 2$. The upstream outcome is a lamella. The orange arrow indicates the direction of pool movement and the scale bar is 2 mm. (c) The result of a simulation matching the conditions in panel (b), with tracer fields used to visualise liquid originating from the droplet and the pool separately. As in the experiment, a lamella is seen upstream. (d) An equivalent oblique impact ($u_o = \sqrt{u_t^2 + u_n^2} = 2.455 \text{ m s}^{-1}$; $\beta = \tan^{-1}(u_t/u_n) = 3.5^\circ$) on a static pool ($u_t = 0 \text{ m s}^{-1}$). The droplet falls from left to right here, in the direction indicated by the green arrow (dashed is vertical). A lamella seen on the leading side, which corresponds to upstream on a moving pool.

an imposed uniform unidirectional velocity field or outflow describing the remaining boundaries. Employing adaptive mesh refinement based on interfacial position location and changes in magnitude of velocity components and vorticity allows us to restrict the computational effort to $O(10^7)$ computational grid cells while maintaining an $O(1) \mu\text{m}$ resolution level for the most resource-intensive flow regions, illustrated in figure 2(a). With these specifications, a typical run that represents approximately 0.5 ms in real time requires $O(10^6)$ CPU hours to complete. A dedicated repository for the source code and typical parametric setup is provided on [GitHub](#). In section 3.6, we use these simulations to compare normal impact on a moving pool with oblique impact onto a static pool.

3. Results and discussion

3.1. Impact outcomes on moving $Ca < 0.2$ pools

Initially, we consider $Ca < 0.2$ impacts, for which a static deep pool produces a SES outcome. Figure 3 shows a representative case ($Ca = 0.132$; 32 vol%) where only the pool speed, $u_t \in \{0, 0.17, 0.26\} \text{ m s}^{-1}$ is varied. As expected, a generally axisymmetric SES is seen for a static pool in figure 3a. The ejecta sheet folding towards the axis of symmetry is clearly visible as an inner circle in the oblique view (bottom row), especially at $t_\mu^* = 5$. For $u_t = 0.17 \text{ m s}^{-1}$ (figure 3b), the dynamics are not axisymmetric, but a SES outcome is maintained in all directions. However, when the pool speed is increased further to $u_t = 0.26 \text{ m s}^{-1}$ (figure 3c), the ejecta sheet develops into a lamella upstream. This outcome is typically seen on viscous ($Ca > 0.2$) or shallow (Sykes *et al.* 2023) static pools. A SES is maintained downstream and in most directions (see the oblique view) except for $\sim 70^\circ$ around the upstream side. That is, above a critical pool speed, the upstream impact outcome transitions from a SES to a lamella.

3.2. Delineating the upstream transition boundary

The Capillary number is the appropriate quantity to represent droplet impact on deep pools (Agbaglah *et al.* 2015). To delineate the upstream transition, we also need to determine a suitable dimensionless quantity to represent pool movement. Thoroddsen *et al.* (2011) developed a simple geometric model to describe ejecta sheet dynamics, in which the ejection velocity is directed tangentially to a sphere approximating the droplet and is

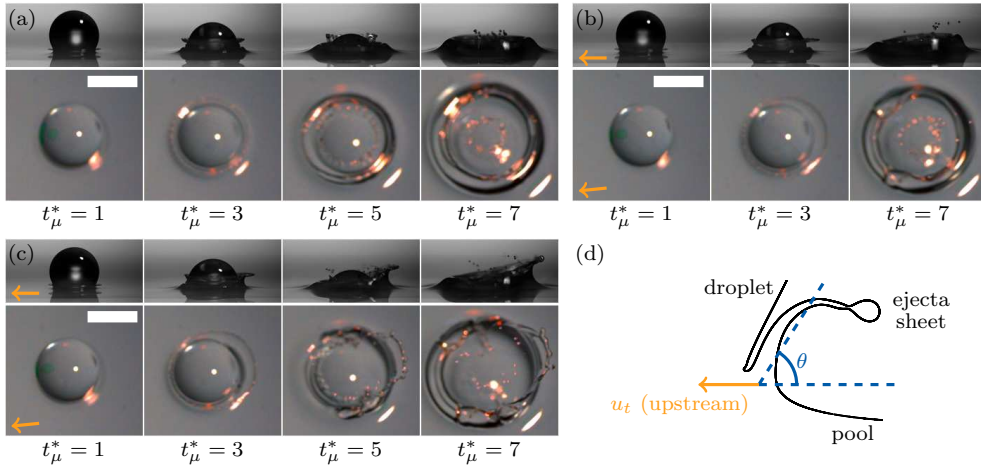


Figure 3. (a)–(c) $Ca = 0.132$ ($We = 345$; $u_n = 3.10$ ms $^{-1}$) impact of a 32 vol% droplet onto a 32 vol% deep pool. (a) The pool is static: separate ejecta sheet, which is expected since $Ca < 0.2$ (figure 1a). (b) The pool moves with $u_t = 0.17$ m s $^{-1}$ ($\sqrt{u_t/u_n} = 0.23$): separate ejecta sheet, but the ejecta sheet dynamics are not axisymmetric. (c) The pool moves with $u_t = 0.26$ m s $^{-1}$ ($\sqrt{u_t/u_n} = 0.29$): lamella upstream and a separate ejecta sheet downstream. (d) Sketch of an ejecta sheet, where θ is the ejecta sheet angle, as defined in Thoraval *et al.* (2012). Orange arrows indicate the direction of pool movement and all scale bars are 2 mm.

proportional in magnitude to $u_n \cos \theta$. Here, θ is the angle between the horizontal and the normal to the ejecta sheet base (carefully defined in Thoraval *et al.* 2012), as sketched in figure 3d. Geometrically, θ is also the angle subtended at the sphere/droplet centre by the droplet impact velocity vector (vertical in the case of normal impact) and radial line to the ejecta sheet base (see figure 8a inset in Thoroddsen *et al.* 2011). In our work, the pre-impact droplet and pool velocity vectors are orthogonal; the resultant velocity vector is directed β from the vertical, where $\tan \beta = u_t/u_n \approx \beta$ since $u_t \ll u_n$. For a geometrically-equivalent oblique impact at an angle β from the vertical on a static pool (discussed further in section 3.6), the “leading side” (adopting the nomenclature of Reijers *et al.* 2019) is equivalent to upstream, which can be understood by considering that a normally-impacting droplet would appear to be falling backwards by an observer travelling on a moving pool. Therefore, for a β oblique impact, θ is effectively reduced, as the droplet impact velocity vector is no longer vertical – it is pointed towards the leading side. Thoraval *et al.* (2012) found that θ increases as $\theta \sim \sqrt{Re} \propto u_n^{1/2}$ for a static deep pool. Here $u_t/u_n \approx \beta$, where β is a constant for a given impact, and therefore suggests that u_t may act inversely proportional to u_n in relation to the evolution of θ upstream on a moving pool, i.e. $\theta^{-1} \sim u_t^{1/2} \propto \sqrt{Re_t} = \sqrt{\rho u_t D/\mu}$. That is, pool movement constrains the growth of θ upstream, although this is practically unmeasurable from our experiments. However, the same conclusion can be reached mechanistically by considering the ejecta sheet base moves with the pool whilst the ejecta sheet evolves, which for an otherwise static ejecta sheet would reduce θ as sketched in figure 3d. This analysis hints at the importance of the non-dimensional quantity $\sqrt{Re_t/Re} = \sqrt{u_t/u_n}$.

Figure 4a shows a regime map of Ca against $\sqrt{u_t/u_n}$, with each data point colour and shape indicating the observed upstream impact outcome (green triangle for SES; red circle for lamella). This regime map contains *all* of the experimental conditions described in section 2.1, including a wide range of fluid properties (see figure S2 in the supplementary material), droplet diameters, and pool & droplet velocities. Together, Ca and $\sqrt{u_t/u_n}$ near

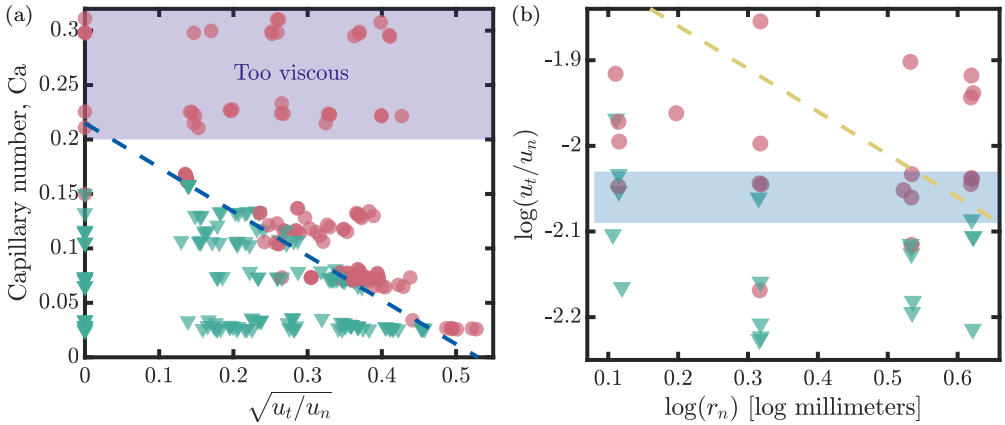


Figure 4. Upstream impact outcomes for normal droplet impact on a moving deep pool. Red circular markers indicate a lamella, while green triangular markers indicate a separate ejecta sheet. (a) This regime map includes all experimental conditions described in section 2.1: $We \in [134, 450]$ and $Re \in [940, 7930]$. The same regime map with markers coloured by the fluid involved is provided as supplementary material. The blue dashed line delineates a linear least squares fit to the transition. (b) $Ca = 0.072 \pm 0.002$ (21 vol% and 1 cSt fluids) with $r_n \in [1.11, 1.87]$ mm to assess the influence of length scale. The blue patch indicates the approximate upstream transition identified. For comparison, the yellow dashed line indicates a $1/4$ exponent (an arbitrary example of a weak dependence for demonstrative purposes) dependence on r_n , i.e. $r_n^{1/4} \sqrt{u_t/u_n}$ for fixed Ca .

perfectly separate all upstream impact outcome types, producing a sharp boundary for $Ca < 0.2$. Note that there is no upstream transition (for all studied pool speeds) when $Ca > 0.2$, which is expected as the impact outcome is already a lamella on a static pool.

Visually, the $Ca < 0.2$ transition boundary appears linear, so it is tempting to attempt a least-squares linear fit. Practically, we do this for all the data (except silicone oils) for which $Ca < 0.15$, in Ca bins of 0.01, fitting to the midpoint of the first lamella and last SES outcome (when increasing pool speed), the extent of which is commensurate to the error in determining $\sqrt{u_t/u_n}$. The result is the blue dashed line in figure 4a, which is consistent with the $Ca \approx 0.16 \pm 0.01$ silicone oil data. Most notably, the fit approximately recovers the known $Ca = 0.2$ static deep pool threshold (Agbaglah *et al.* 2015), so a single constant (representing the gradient, ≈ -0.4) delineates the upstream transition alongside Ca and $\sqrt{u_t/u_n}$. Intriguingly, neither of these two quantities contain a length scale, despite the experiments in figure 4a having $D \in [2.20, 3.75]$ mm. This observation suggests that the upstream transition is length-scale invariant, which we now investigate.

3.3. Length-scale invariance of the upstream transition

To assess the involvement of the length scale in the upstream transition, we consider experiments with a fixed Ca across the full range of $D = 2r_n$ studied. We suppose that $r_n^\alpha \sqrt{u_t/u_n} = c$, where c is a constant, and α is an unknown exponent to be determined. Hence, $\log(u_t/u_n) = -2\alpha \log(r_n) + 2 \log(c)$, so -2α would be the upstream transition gradient on a graph of $\log(u_t/u_n)$ against $\log(r_n)$ for fixed Ca . Such a graph (for fixed $Ca = 0.072 \pm 0.002$; 21 vol% and 1 cSt fluids) is shown in figure 4b. Within the expected experimental error, the upstream transition appears flat (indicated within the blue patch), suggesting that $\alpha = 0$. By way of comparison, the orange dashed line delineates the expected transition for a relatively weak length-scale dependence of $\alpha = 0.25$ (an arbitrary choice), which is fixed at the bottom of the blue patch on the right-hand side. This analysis strongly suggests that the upstream transition is length-scale invariant.

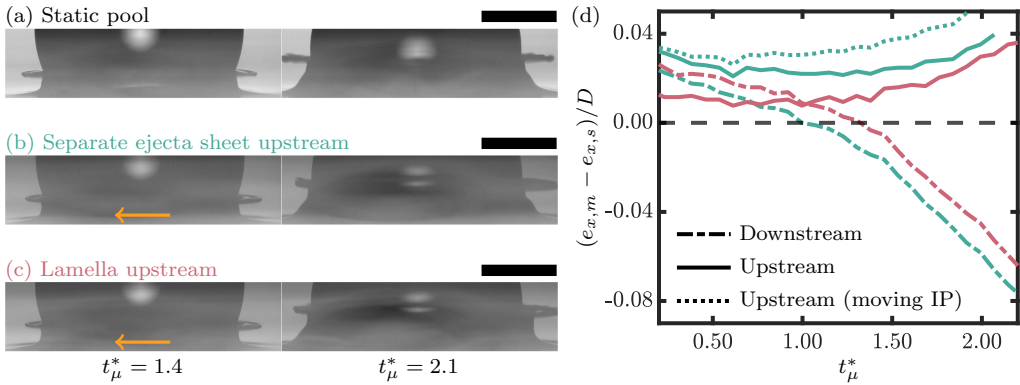


Figure 5. (a)–(c) High resolution ($327 \text{ pixels mm}^{-1}$) images of the early-time ejecta sheet dynamics of $Ca = 0.115 \pm 0.002$ impact (32 vol% fluid). (a) Static pool. (b)–(c) $u_t = 0.20 \pm 0.01 \text{ m s}^{-1}$ ($\sqrt{u_t/u_n} = 0.27$): (b) separate ejecta sheet upstream; (c) lamella upstream. Orange arrows indicate the direction of pool movement and all scale bars are 1 mm. (d) Data indicating the difference between the horizontal extent of the ejecta sheet on moving and static pools, from the experiments in panels (a)–(c). $e_{x,p}$ is the horizontal position of the ejecta sheet tip from the original impact point (IP); $p = m$ for a moving pool (either (b) green or (c) red) and $p = s$ for a static pool. In one case (*moving IP*, dashed line), the IP is translated with the moving pool speed over time.

3.4. Ejecta sheet dynamics

To attain a detailed view of the early-time ejecta sheet dynamics, the side-view camera was replaced by a Phantom TMX 5010 (110,000 fps; $1.0 \mu\text{s}$ exposure) equipped with a Navitar 12X Zoom lens (for $327 \text{ pixels mm}^{-1}$) for the experiments in figure 5. Here, $Ca = 0.115 \pm 0.002$ (32 vol% fluid), with a SES outcome on a static pool (figure 5a). For both figures 5b and 5c, u_t was set such that $\sqrt{u_t/u_n} = 0.27$, which is approximately the upstream transition threshold according to figure 4a. Figure 5b shows a SES upstream (i.e. before the transition); figure 5c a lamella upstream (i.e. after the transition).

Qualitatively, the ejecta sheets appear similar at $t_\mu^* = 1.4$, whether the pool is static or moving. However, the vortex separation process that produces a SES outcome is known to start at $t_\mu^* = 1.05$ (Agbaglah *et al.* 2015), which must be inhibited upstream in figure 5c to generate the lamella outcome. It appears that the ejecta sheet is slightly thicker on the moving pools in figure 5, although this cannot be systematically confirmed within reasonable error tolerances with our current experimental and numerical setups. By $t_\mu^* = 2.1$, the impact outcomes are visually evident and the ejecta sheet has notably different horizontal extents from the impact point, $e_{x,p}$ ($p = m$ moving; $p = s$ static) upstream and downstream. These observations are confirmed quantitatively in figure 5d. Around the aforementioned $t_\mu^* = 1.05$, the ejecta sheet considerably shortens downstream, relative to a static pool (so $e_{x,m} < e_{x,s}$), when the pool is moving. Upstream, the ejecta sheet is always stretched (so $e_{x,m} > e_{x,s}$), even when measuring $e_{x,m}$ from the fixed impact point (dash-dot and solid lines). However, pool movement translates the impact point downstream, which conceivably augments ejecta sheet stretching upstream. To account for this effect, $e_{x,m}$ can be measured from the moving impact point (practically, adding $24 \mu\text{m}$ per t_μ^* time unit to $e_{x,m} - e_{x,s}$), which is shown in figure 5d as a dotted line for the upstream side of the figure 5b data. These analyses indicate that the ejecta sheet is considerably stretched upstream on a moving pool, which raises the prospect that pool movement thins the ejecta sheet at its base and restricts flow into it from the pool. It is this mechanism that we found to yield a lamella on sufficiently shallow pools in our previous work (Sykes *et al.* 2023),

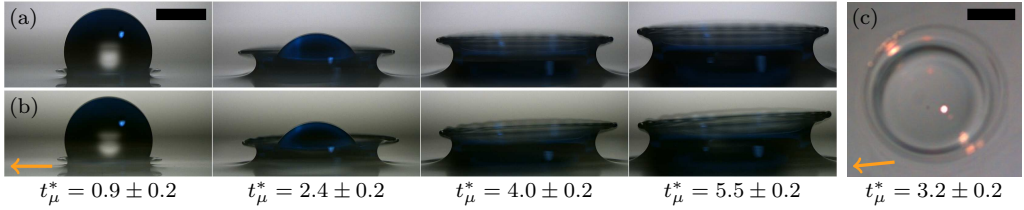


Figure 6. $Ca = 0.213 \pm 0.002$ with the 43 vol% fluid. (a) Static pool. (b)–(c) Moving pool with $\sqrt{u_t/u_n} = 0.33$. The blue tinge in (a) and (b) is an artifact of repeated inner wall surface treatments and the light source. Orange arrows indicate the direction of pool movement and all scale bars are 1 mm.

where ejecta sheet stretching was found to be caused by a pressure confinement effect of the pool base. Hence, similar physical mechanisms may be at play in both configurations.

3.5. Downstream impact outcome

In so far as pool movement effectively constrains the evolution of θ , the opposite is true downstream. Therefore, were the root cause of the upstream transition purely geometric according to section 3.2, we might expect pool movement to recover a SES *downstream* when the static pool impact outcome is a lamella ($Ca > 0.2$). Throughout our experimental campaign, no such transition was seen. Figure 6 exemplifies typical dynamics for $Ca > 0.2$ on static (figure 6a) and relatively fast-moving (figures 6b and 6c, $u_t = 0.29 \text{ m s}^{-1}$) pools. It is notable that little asymmetry can be seen in the side views (e.g. figure 6b), especially at early times. Moreover, the oblique view (figure 6c) shows remarkably smooth dynamics and offers no hint of an instability that is typically apparent with the SES outcome.

Within the limits of the experimental design (namely the limitation on pool speed), our results indicate that there is no lamella to SES transition downstream for $Ca > 0.2$. That is, when the pool is “too viscous” (figure 4a), there is no other outcome than a lamella when the pool boundary layer is negligible. The lack of “reversibility” in the SES-lamella transition hints at a fundamental idea relevant to both moving and static pools: the cause of the transition is not purely geometric. Rather, the association of the transition to $t_\mu^* = 1.05$ (first made by Agbaglah *et al.* 2015) appears causal, hinting that the root cause of a SES is an instability at the base of the ejecta sheet that enables vortex shedding. For $Ca > 0.2$, viscosity suppresses the instability and the ability to attain the SES outcome.

3.6. Oblique impact

Except the presence of a boundary layer on the moving pool, prior to coalescence normal droplet impact onto a moving pool is geometrically equivalent to oblique impact on a static pool at an angle β from vertical and a velocity u_o , where $u_n = u_o \cos \beta$ and $u_t = u_o \sin \beta$. On solid surfaces, the two types of impact are equivalent regarding the resulting spreading and splashing behaviour (Buksh *et al.* 2020). The boundary layer on moving pools is known to have qualitative effects on impact outcomes when $u_t \gtrsim u_n$, and can even support the weight of an impacting droplet so that it ‘surfs’ without coalescing (Castrejón-Pita *et al.* 2016). Of course, the persistent effect of pool movement does affect longer timescale dynamics, such as bouncing, compared to an oblique impact on a static pool (Harris *et al.* 2025). However, when $u_n \ll u_t$ we hypothesise that the boundary layer does not play a decisive role on the ejecta sheet dynamics, so we expect a transition on the leading side (equivalent to upstream on a moving pool, see section 3.2) of a sufficiently oblique impact.

Previously, oblique impacts of small droplets ($115 \pm 15 \mu\text{m}$) have been achieved via deflection with an electric field, which is a process used in some commercial continuous

inkjet printers. The resulting long timescale dynamics (e.g. crown shape and Worthington jet inclination) appear qualitatively similar to our asymmetric moving pool experiments (Gielen *et al.* 2017). However, the greater inertia of larger droplets in our study makes highly-controlled oblique impacts challenging to engender experimentally, so we turn to simulations that have been used to successfully study oblique impacts previously (Cimpeanu & Papageorgiou 2018). We reproduced the experiment in figure 2b ($Ca = 0.105$, 32 vol%, $u_n = 2.45 \text{ m s}^{-1}$, $u_t = 0.15 \text{ m s}^{-1}$) computationally in figure 2c, with good qualitative agreement. The equivalent oblique impact has $u_o = 2.455 \text{ m s}^{-1}$ (to 3 decimal places) and $\beta = 3.5^\circ$. This very small angle is shown diagrammatically (as green arrows) inset in figure 2d, alongside the results of the equivalent oblique impact simulation. As predicted, a lamella is formed on the leading side rather than the SES outcome, supporting our rationale that the moving pool boundary layer does not play a decisive role. This result indicates that our findings for moving pools are generalisable to equivalent oblique impacts.

4. Conclusions

For $Ca < 0.2$ normal impacts on deep pools, the typical separate ejecta sheet dynamics transition to a lamella only upstream, above a critical pool speed. Such asymmetric outcomes arise with little pool movement (e.g. above a pool-droplet velocity ratio of $u_t/u_n = 0.08$ when $Ca = 0.10$), raising the prospect that the motion of rivers and oceans may result in asymmetric raindrop impact. The transition boundary is well-parametrised by Ca and $\sqrt{u_t/u_n}$, which are both independent of length scale. By considering experiments with a fixed Ca , we concluded that the upstream transition is length-scale invariant. We explained the importance of the $\sqrt{u_t/u_n}$ physically as a constraining effect of pool movement on the ejecta sheet angle evolution upstream. A linear fit to the transition boundary recovers the known $Ca = 0.2$ threshold on static deep pools (Agbaglah *et al.* 2015). No reverse transition (lamella to separate ejecta sheet) is seen downstream for $Ca > 0.2$, which suggests that the underlying mechanism causing the separate ejecta sheet outcome is not purely geometric. Instead, our results suggest an instability (characterised by the visco-capillary time scale) that is suppressed by high viscosity; this conclusion applies to any like-fluid pool impact. Our 3D DNS framework enabled us to confirm similar dynamics for an equivalent oblique impact on a static pool, suggesting that the moving pool boundary layer does not have a decisive role on impact outcomes when $u_t \ll u_n$. Our findings offer insight into common natural and industrial scenarios (e.g. ocean air-sea exchange, inkjet printing) involving moving pools where satellite droplet production is often an important consideration, as well as contributing to the fundamental understanding of the physical mechanisms that determine impact outcomes on pools more generally.

Supplementary Material. Supplementary material are available at [URL to be inserted by publisher].

Acknowledgments. We thank Prof. Peter Read (Oxford Physics) for lending the rotating table base, Duncan Constable (Oxford Engineering) for helping to manufacture the annular tank, and Oliver Sand for setting up the rotating table at Brown.

Funding. This work was funded by the US National Science Foundation (NSF CBET-2123371), UK Engineering and Physical Sciences Research Council (EP/W016036/1), and the John Fell Fund (0014320).

Data availability. Data are available at <https://github.com/OxfordFluidsLab/MovingPoolImpact>.

Declaration of interests. The authors report no conflict of interest.

REFERENCES

- AGBAGLAH, G., THORAVAL, M.-J., THORODDSEN, S.T., ZHANG, L.V., FEZZAA, K. & DEEGAN, R.D. 2015 Drop impact into a deep pool: vortex shedding and jet formation. *J. Fluid Mech.* **764**, R1.
 ANGUELOVA, M.D. 2021 Big potential for tiny droplets. *Nat. Geosci.* **14** (8), 543–544.

- BAO, M., YI, Z., ZHAO, D., LIU, H., GUO, Y., GONG, L. & SHEN, S. 2025 Dynamic characteristics of oblique droplet impact on a liquid film. *Phys. Fluids* **37** (2), 022101.
- BIRD, J.C., TSAI, SCOTT S.H. & STONE, H.A. 2009 Inclined to splash: triggering and inhibiting a splash with tangential velocity. *New J. Phys.* **11** (6), 063017.
- BUKSH, S., MARENGO, M. & AMIRFAZLI, A. 2020 Impacting of droplets on moving surface and inclined surfaces. *Atomization Sprays* **30** (8), 557–574.
- CASTREJÓN-PITA, J.R., MUÑOZ-SÁNCHEZ, B.N., HUTCHINGS, I.M. & CASTREJÓN-PITA, A.A. 2016 Droplet impact onto moving liquids. *J. Fluid Mech.* **809**, 716–725.
- CHENG, N.-S. 2008 Formula for the viscosity of a glycerol–water mixture. *Ind. Eng. Chem. Res.* **47** (9), 3285–3288.
- CIMPEANU, R. & PAPAGEORGIOU, D.T. 2018 Three-dimensional high speed drop impact onto solid surfaces at arbitrary angles. *Int. J. Multiphase Flow* **107**, 192–207.
- CROCKER, J.C. & GRIER, D.G. 1996 Methods of digital video microscopy for colloidal studies. *J. Colloid Interface Sci.* **179** (1), 298–310.
- FUDGE, B.D., CIMPEANU, R., ANTKOWIAK, A., CASTREJÓN-PITA, J.R. & CASTREJÓN-PITA, A.A. 2023 Drop splashing after impact onto immiscible pools of different viscosities. *J. Colloid Interface Sci.* **641**, 585–594.
- GIELEN, M.V., SLEUTEL, P., BENSCHOP, J., RIEPEN, M., VORONINA, V., VISSER, C.W., LOHSE, D., SNOEIJER, J.H., VERSLUIS, M. & GELDERBLOM, H. 2017 Oblique drop impact onto a deep liquid pool. *Phys. Rev. Fluids* **2** (8), 083602.
- GREENSPAN, H.P. & HOWARD, L.N. 1963 On a time-dependent motion of a rotating fluid. *J. Fluid Mech.* **17** (3), 385–404.
- GUO, W., XU, Y., WANG, J., TIAN, C., ZHAO, N. & ZHU, C. 2025 Numerical simulation of multi-angle droplet impact on flowing thin water film and secondary droplet generation. *Phys. Fluids* **37** (10), 103335.
- GUPTA, G. & KUMAR, P. 2020 Splashing dynamics of a drop impact onto a deep liquid pool with moving film interface. *Phys. Fluids* **32** (1), 012102.
- HAO, J. & GREEN, S.I. 2017 Splash threshold of a droplet impacting a moving substrate. *Phys. Fluids* **29** (1), 012103.
- HAO, J., LU, JIE, LEE, LIAONAN, WU, ZHIHU, HU, GENGKAI & FLORYAN, J.M. 2019 Droplet splashing on an inclined surface. *Phys. Rev. Lett.* **122** (5), 054501.
- HARRIS, D.M., ALVENTOSA, L.F.L., SAND, O., SILVER, E., MOHAMMADI, A., SYKES, T.C, CASTREJÓN-PITA, A.A. & CIMPEANU, R. 2025 Bouncing to coalescence transition for droplet impact onto moving liquid pools. *arXiv preprint arXiv:2510.02220*.
- HOMICZ, G.F. & GERBER, N. 1987 Numerical model for fluid spin-up from rest in a partially filled cylinder. *J. Fluids Eng.* **109** (2), 194–197.
- LI, D., SHANG, Y., WANG, X. & ZHANG, J. 2024 Dynamic behavior of droplet impacting on a moving surface. *Exp. Therm Fluid Sci.* **153**, 111126.
- LOHSE, D. 2022 Fundamental fluid dynamics challenges in inkjet printing. *Annu. Rev. Fluid Mech.* **54**, 349–382.
- POPINET, S. 2009 An accurate adaptive solver for surface-tension-driven interfacial flows. *J. Comput. Phys.* **228** (16), 5838–5866.
- POPINET, S. 2015 A quadtree-adaptive multigrid solver for the Serre–Green–Naghdi equations. *J. Comput. Phys.* **302**, 336–358.
- REIJERS, S.A., LIU, B., LOHSE, D. & GELDERBLOM, H. 2019 Oblique droplet impact onto a deep liquid pool. *arXiv preprint arXiv:1903.08978*.
- STUMPF, B., QEZELIEH, S.A., KAMAL, R., DEZITTER, F., MARTUFFO, A., ROISMAN, I.V. & HUSSONG, J. 2025 Drop impact onto a moving substrate: Aerodynamic rebound. *Int. J. Multiphase Flow* **184**, 105113.
- SYKES, T.C., CIMPEANU, R., FUDGE, B.D., CASTREJÓN-PITA, J.R. & CASTREJÓN-PITA, A.A. 2023 Droplet impact dynamics on shallow pools. *J. Fluid Mech.* **970**, A34.
- THORAVAL, M.-J., TAKEHARA, K., ETOH, T.G., POPINET, S., RAY, P., JOSSERAND, C., ZALESKI, S. & THORODDSEN, S.T. 2012 von Kármán vortex street within an impacting drop. *Phys. Rev. Lett.* **108** (26), 264506.
- THORODDSEN, S.T. 2002 The ejecta sheet generated by the impact of a drop. *J. Fluid Mech.* **451**, 373–381.
- THORODDSEN, S.T., THORAVAL, M.-J., TAKEHARA, K. & ETOH, T.G. 2011 Droplet splashing by a slingshot mechanism. *Phys. Rev. Lett.* **106** (3), 034501.
- WANG, H., LIU, S., BAYEUL-LAINÉ, A.-C., MURPHY, D., KATZ, J. & COUTIER-DELGOSHA, O. 2023 Analysis of high-speed drop impact onto deep liquid pool. *J. Fluid Mech.* **972**, A31.
- WEISS, D. A. & YARIN, A. L. 1999 Single drop impact onto liquid films: neck distortion, jetting, tiny bubble entrainment, and crown formation. *J. Fluid Mech.* **385**, 229–254.